Au/MoS$_2$ tips as auxiliary rate aligners for the photocatalytic generation of syngas with a tunable composition

Xuemin Hu [a,b], Jie Jin [d], Yuqing Wang [c], Cheng Lin [b], Shipeng Wan [b], Kan Zhang [b,*], Luyang Wang [c,**], Jong Hyeok Park [d,**]

[a] *School of Material Engineering, Jinling Institute of Technology, Nanjing 211169, PR China*
[b] *College of Materials Science and Engineering, Nanjing University of Science and Technology, Nanjing 210094, PR China*
[c] *College of New Materials and New Energies, Shenzhen Technology University, Shenzhen, Guangdong 518118, PR China*
[d] *Department of Chemical and Biomolecular Engineering, Yonsei University, 50 Yonsei-ro, Seodaemun-gu, Seoul 120-749, Republic of Korea*

ARTICLE INFO

ABSTRACT

Synthesis gas (syngas), with a wide range of molar ratios of CO and H$_2$ from 0.3 to 4, can serve as an important feedstock in the petroleum industry for the production of various synfuels; however, it remains a major challenge to tune the composition over such a wide range of ratios. Here, we demonstrate the photocatalytic production of syngas with tunable H$_2$/CO molar ratios via rationally designed Au/MoS$_2$ symmetrically tipped CdS nanowires (AMTCs), in which MoS$_2$ and Au serve as cocatalysts for the hydrogen evolution reaction (HER) and CO$_2$ reduction reaction (CO$_2$RR), respectively. The competing reactions are controlled and aligned through the selective decoration of size-controlled (1–50 nm) Au nanoparticles on MoS$_2$ by controlling the charge transfer kinetics during photodeposition. Finally, the widest range of H$_2$/CO ratios in syngas reported to date, ranging from 0.35 to 3.6, is realized, indicating that this is a potentially efficient approach for solar-to-syngas production by using rationally designed nanostructures.

1. Introduction

Energy and environmental crises have resulted in considerable efforts being directed toward converting natural solar energy to chemical fuel because it is the cleanest, greenest, and most efficient strategy [1–3]. Of particular interest in solar-to-fuel conversion are the H$_2$ evolution reaction (HER) and CO$_2$ reduction reaction (CO$_2$RR), in which a suitable photocatalyst-cocatalyst pair typically drives targeted photocatalysis [4,5]. Because the HER and CO$_2$RR occur in an aqueous solution and generally exhibit strong competition, the ability to tune the molar ratio of H$_2$ to CO in the synthesis gas (syngas) products to values from 0.3 to 4 has received considerable attention in photocatalysis and electrocatalysis fields [6–8]. Since the applied bias affects the activation energies and rate constants of the HER and CO$_2$RR to different degrees in electrocatalysis, the syngas compositions can be tuned by taking advantage of the applied bias-dependent activity. However, the intrinsic bandgap energy (E$_g$) and activation overpotential of photocatalysts make it difficult to tune the syngas composition when using a single

cocatalyst. As a result, the cocatalyst must generally have two components to drive the HER and CO$_2$RR and enable tuning of the syngas composition during photocatalysis [9–11]. The interfaces of different cocatalysts and photocatalysts are so complex that the photocharge transfer from photocatalyst to cocatalyst required to align HER and CO$_2$RR ratios is an open question.

Thus far, a constant interfacial charge transfer from the photocatalyst to the cocatalyst beyond random electron flow has been well demonstrated in Au- or Pt-tipped CdS nanowires (NWs) [12–17], in which photoinduced electrons can directionally migrate and accumulate at the tip domain to maintain a long-lived charge-separated state [18–24]. Then, the design concept of constant interfacial charge transfer was expanded to several materials, such as amorphous TiO$_2$-tipped Au NRs [25], Pt-tipped CdSe NRs [26], Pt-tipped Cu$_2$S NRs [27], and Pd/Au alloy-tipped CdS NRs [28], which have been successfully applied in the photocatalytic HER or CO$_2$RR. Nevertheless, exploring the tipping of two- or multicomponent cocatalysts with 1D photocatalysts possessing multifunctional properties that can align the reaction rates of the HER
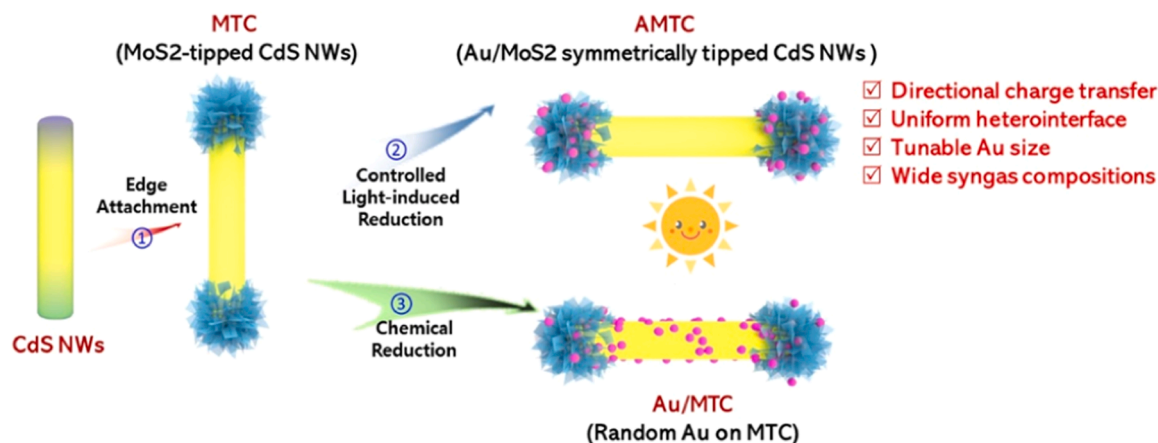
Fig. 1. Synthetic schemes. (1) Oriented attachment based on the high reactivity of the S- or Cd-terminated (001) facet of CdS NWs due to chemical asymmetry. (2) Photoinduced electron migration from CdS to the Au tips achieved deposition of metallic Au at the NW apexes (50 mg MTC in 5 μL (5 mmol) HAuCl₄ solution under light irradiation at 520 nm for 20 min). (3) Chemically reduced Au was randomly dispersed on MTC (50 mg MTC in 5 μL (5 mmol) HAuCl₄ solution using hydrazine hydrate as the reduction agent)

and CO₂RR is an attractive goal for synthetic chemistry and energy science [29–32].

In this work, the ability of Au/MoS₂ symmetrically tipped CdS nanowires (NWs) with a uniform interface to serve as an auxiliary rate aligner of the photocatalytic HER and CO₂RR to enable tuning of the syngas composition is demonstrated. We report here that controlling the size of Au particles and optimizing the electrolyte composition are the key parameters. The highly selective loading of Au onto MoS₂ tips decreases the MoS₂ work function through electron injection, which therefore reduces the energy barrier of the MoS₂/CdS interface and facilitates the photoinduced charge transfer from CdS NWs to Au/MoS₂. Moreover, we can tune the reaction kinetics for the HER and CO₂RR by controlling the size of the Au particles, and the CO product selectivity of the CO₂RR can be optimized by tuning the charge migration rate in KHCO₃/triethanolamine (TEOA) aqueous electrolyte, eventually achieving a tunable syngas composition with H₂/CO ratios ranging from 0.35 to 3.6.

2. Experimental section

2.1. Synthesis of Au/MoS₂-tipped CdS NW

The MoS₂-tipped CdS NWs were synthesized based on our previous procedure, and the optimized weight ratio of MoS₂ was 17.4% [24]. Fifty milligrams of 17.4 wt% MoS₂-tipped CdS NWs were dispersed into 25 mL H₂O/25 mL formic acid, methanol, lactic acid or triethanolamine or 50 mL 0.5 M Na₂SO₃ or ethylenediaminetetraacetic acid disodium salt mixture via ultrasonication. Then, 5 μL (5 mmol) HAuCl₄ aqueous solution was added. The solution was transferred to a quartz reactor and illuminated under 520 nm monochromatic light irradiation for 20 min (11.7 mW/cm²). The Au/MoS₂-tipped CdS NW product was obtained and washed with water and ethanol several times, and annealed at 400 °C for 2 h under Ar. The Au/CdS hybrid was prepared by a similar procedure with CdS NWs instead of MoS₂-tipped CdS NWs. For comparison, 50 μL hydrazine hydrate was added to the mixed 17.4 wt% MoS₂-tipped CdS NWs and 5 μL (5 mmol) HAuCl₄ in 25 mL H₂O/25 mL lactic acid solution. After stirring for 2 h, the Au-loaded MoS₂-tipped CdS NWs were collected and washed with water and ethanol several times, and annealed at 400 °C for 2 h under Ar.

2.2. Characterization

Field emission scanning electron microscopy (FE-SEM) images were taken with an FEI Quanta 250 FEG scanning electron microscope.

Transmission electron microscopy (TEM) observations were carried out on a JEOL JEM-AFM 200 F (Japan) electron microscope with Cs-corrected/energy-dispersive X-ray spectroscopy (EDS)/EELS. X-ray diffraction (XRD) was carried out with a Bruker-AXS D8 Advance diffraction system with a Cu Kα source (λ = 1.54056 Å). X-ray photoelectron spectroscopy (XPS) was recorded on an Auger electron spectroscopy (AES) XPS instrument (ESCA 2000 from VG Microtech in England) equipped with an aluminium anode (Al Kα, λ = 1486.6 eV). The absorption spectra were detected with a Shimadzu UV-3600 equipped with an integrating sphere. The concentration of Au ions in reaction solution was measured by inductively coupled plasma-optical emission spectrometry (ICP-OES, Agilent 720ES).

In situ diffuse reflectance infrared Fourier transform spectra (DRIFTS) were measured by using FT-IR spectrometry with a designed reaction cell. The reactor was first purged with N₂ at 150 °C and a flow rate of 50 mL/min. After cooling to room temperature, high-purity CO₂ was pumped in for CO₂ adsorption. The IR signals were collected in dark and under visible light irradiation, respectively. CO₂ temperature programmed desorption (TPD) experiments were carried out by first purging with He at 100 °C for 30 min and then cooling to 50 °C. After pumping excess CO₂ away, the samples were heated to 350 °C at a rate of 10 °C/min to record the desorption spectra during heating.

The isotope labeling measurements were carried out by using ¹³CO₂ gas (isotope purity, 99%, and chemical purity, 99.9%) as the reaction source and gas chromatography-mass spectrometry (7890 A GC system, USA; 5 Å molecular sieve columns). Low-temperature PL spectra was recorded using a monochromator (SP-2150i, Acton) combined with a photomultiplier tube (PD-174, Acton) and spectrofluorometer (Hitachi F-7000) with a xenon lamp under vacuum at 10 K.

For electrocatalytic tests, the electrodes were fabricated onto a plant glassy carbon (GC) electrode, and the slurry was prepared by mixing catalyst (4 mg) and Nafion solution (30 mL; Sigma-Aldrich, 5 wt%) in a solution of water/ethanol (1 mL; 3:1 v/v), the loading mass was 0.285 mg/cm². Electrocatalytic CO₂ reduction was conducted in 0.5 M KHCO₃ electrolyte (purged with pure CO₂) under 200 rpm stirring using a Ag/AgCl (in 3 M KCl solution) electrode as the reference electrode, Electrocatalytic H₂ evolution was conducted in 1 M lactic acid.

All of the potentials were calibrated to an RHE:

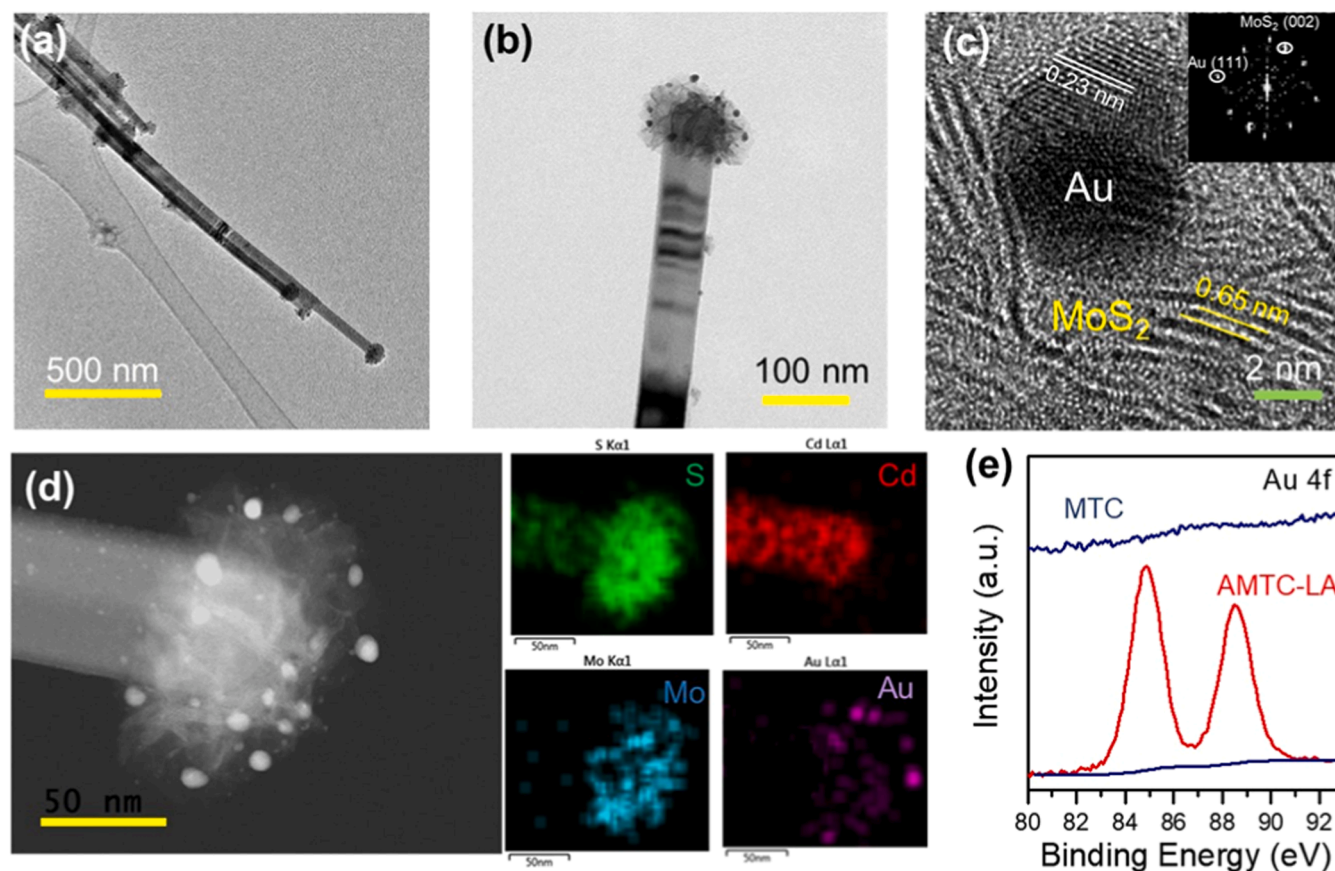RHE= Applied potential + 0.197 V + 0.0592×pH

Fig. 2. (a) TEM image of Au/MoS$_2$-tipped CdS NWs (AMTC-LA). (b and c) TEM and HR-TEM images of AMTC-LA. (d) Element mapping of AMTC-LA. (e) Au XPS spectra of MTC and AMTC-LA. Inset in Fig. 2c is the fast Fourier transform (FFT) pattern.

2.3. Photocatalytic H$_2$ generation and CO$_2$ reduction

The photocatalytic experiment was performed with a commercial online automatic testing system (Perfectlight Sci&Tech Co., Ltd., Labsolar-6A) connected to a gas chromatography system (PerkinElmer, Clarus 580, USA) with a FID detector to analyze CO and a TCD detector to analyze H$_2$. A solar simulator (300 W Xe Lamp) with a UV-cutoff filter ($\leq$420 nm) was employed as the light source. The photocatalytic reduction experiments were conducted in a 30 mL reaction chamber using ~0.25 mg photocatalyst. For H$_2$ generation, H$_2$O/lactic acid at a ratio of 1:1 vol was used as an electrolyte and then purged with N$_2$ gas for 30 min. For CO$_2$ reduction, 0.5 M KHCO$_3$ with different hole scavengers was used as an electrolyte and then purged with CO$_2$ gas for 30 min

2.3.1. Quantum efficiency calculation

The apparent quantum efficiency was calculated from the following equation:

$$QE = \frac{2 \times Number\ of\ evolved\ H_2\ molecules}{the\ number\ of\ incident\ photons} \times 100\%$$

At 420 nm, the intensity of irradiation was determined to be 1.12 mW/cm^2 by Oriel P/N 91150 V spectroradiometer (VLSI standards) and the total area of irradiation was 1.77 cm^2. After 5 h irradiation, the H$_2$ and CO amounts were estimated to be 0.179 and 0.502 mmol, respectively under 420 nm wavelength irradiation. The total gas evolution rate is 1.362 μmol/h.

The number of incident photons (N) is around 3.6×10^{20} according to the equation of $N = \frac{E\lambda}{hc}$.

Thus, $AQY = \frac{2 \times 6.02 \times 10^{23} \times 1.362 \times 10^{-6}}{3.6 \times 10^{20}} = 45.55\%$.

3. Results and discussion

3.1. Synthesis and characterization of photocatalyst

The synthetic procedure is schematically illustrated in Fig. 1. First, 17.4 wt% MoS$_2$-tipped CdS (MTC) NWs, with exhibited the best photocatalytic performance, was synthesized via oriented attachment growth according to our previous report [25] and was subsequently used as a platform for Au deposition. FE-SEM images of individually synthesized MoS$_2$ and CdS NWs (Fig. S1) show flower-like MoS$_2$ spheres and 1D CdS NWs, respectively. FE-SEM and high-angle annular dark-field scanning TEM (HAADF-TEM) analyses of the 17.4 wt% MTC demonstrate a centrosymmetric structure with spherical MoS$_2$ tips and CdS stems (Fig. S2). Inspired by Au-tipped CdS NRs under light illumination that induced overgrowth of the Au domains and deposition of other components via photoreduction [33], we performed highly MoS$_2$ tip-selective deposition of Au under mild light-induced reduction conditions in the presence of lactic acid (LA) electrolyte (see experimental section for details). For comparison, random deposition of Au on MTC (Au/MTC) was carried out by chemical reduction in the presence of lactic acid (LA) electrolyte. TEM images of typical Au/MoS$_2$-tipped CdS NWs synthesized in LA electrolyte (AMTC-LA) are shown in Fig. 2a and S3, indicating that most of the centrosymmetric sharpness of MTC NWs is inherited, except for the obvious appearance of bright Au dots at the MoS$_2$ tips. XRD patterns of AMTC-LA clearly show a diffraction peak at 38.2° that was not in the pattern of MTC; this new peak is characteristic of the Au (111) plane in JCPDS no 04–0784 (Fig. S4). The enlarged TEM image of AMTC in Fig. 2b shows that Au nanoparticles with a diameter of ~10 nm were precisely deposited on the MoS$_2$ tips. A high-resolution TEM (HR-TEM) image reveals that these Au nanoparticles are anchored on the MoS$_2$ surface, where the lattice spacing of Au is 0.23 nm,
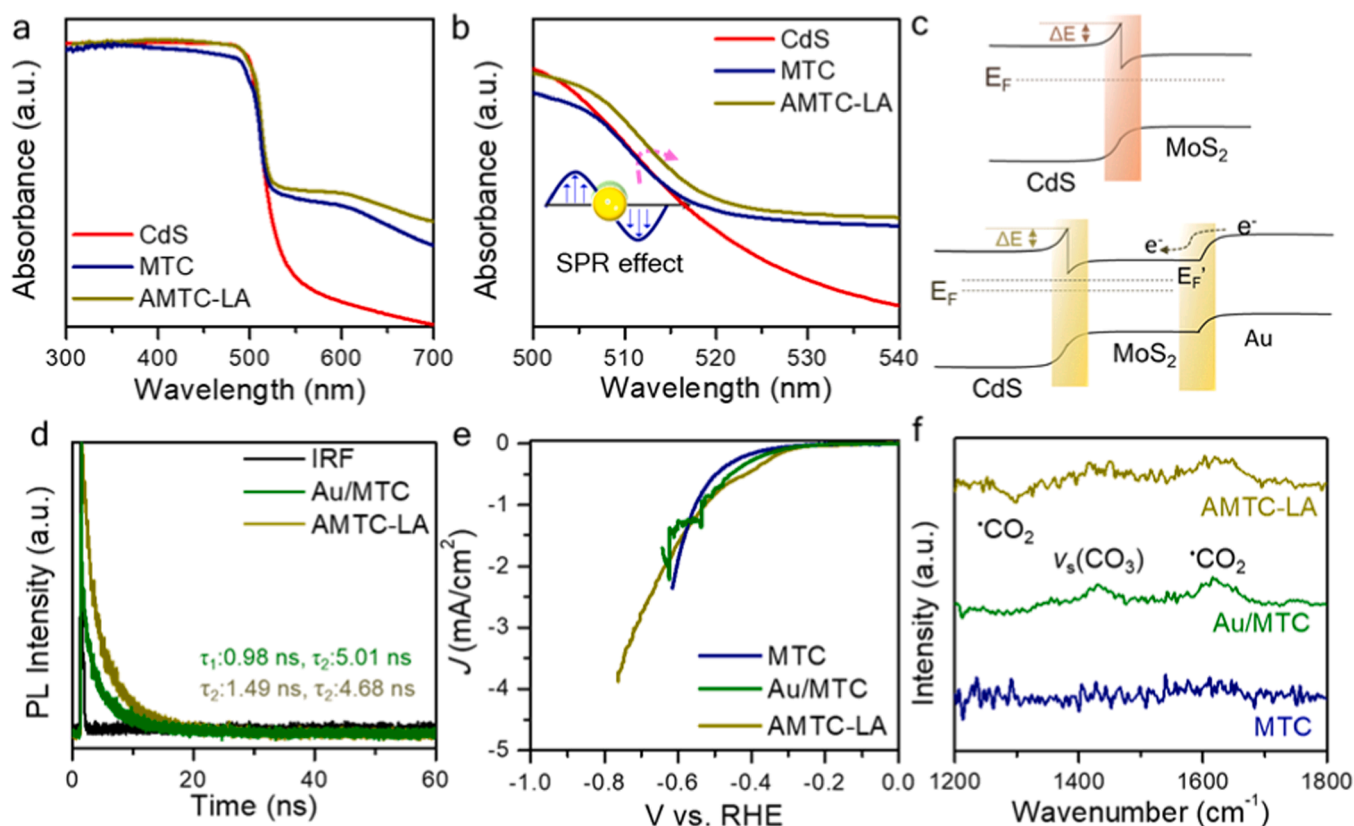
Fig. 3. (a and b) UV–vis absorption spectra of CdS NWs, MTC, and AMTC-LA. (c) Band diagrams of MTC and AMTC-LA. (d) PL decay profiles of Au/MTC, and AMTC-LA from 400 nm excitation at 20 K. The monitored wavelength was 491 nm. PL decay curves were fitted by a biexponential function to calculate the sample lifetimes. The intensity-weighted average exciton lifetime was $f_1\tau_1 + f_2\tau_2$, where f_1 and f_2 are fractional intensities and τ_1 and τ_2 are lifetimes. (e) Polarization curves of the MTC, Au/MTC, and AMTC-LA electrodes in 0.5 M KHCO$_3$ (purged with CO$_2$) under 200 rpm stirring; the curves were collected at a scan rate of 5 mV/s. (f) In situ DRIFTS for CO$_2$ activation over MTC, Au/MTC, and AMTC-LA in the dark.

corresponding to the presence of a (111)-dominated facet (Fig. 2c). The fast Fourier transform (FFT) pattern (inset of Fig. 2c) confirms the coexistence of the (111) plane of Au and the (002) plane of MoS$_2$. HAADF-STEM energy-dispersive X-ray spectroscopy (EDX) analyses demonstrate that the Au nanoparticles are concentrated on the MoS$_2$ tips, while Cd is present in only the stem part (Fig. 2d). Fig. 2e compares the high-resolution XPS data on Au 4 f for MTC and AMTC-LA. The two peaks at 84.8 and 88.5 eV appearing in the Au spectrum of AMTC-LA correspond to metallic Au [34]. The highly MoS$_2$ tip-selective deposition of Au under mild light-induced reduction conditions suggests that the photoinduced electrons from excited CdS NWs mainly accumulate at MoS$_2$ tips, which is in sharp contrast to the random distribution of Au when directly photodeposited on CdS NWs (Au/CdS-LA) (Fig. S5). Furthermore, the highly MoS$_2$ tip-selective deposition of Pt can also be achieved by photoinduced electron accumulation (Fig. S6), while the photoinduced hole migrates to the CdS NW stem (Fig. S7). A CdS NW structure tipped with both Au and MoS$_2$ would possess a homogeneous interface for photoinduced charge transfer.

3.2. Optical and electrocatalytic properties of photocatalyst

The UV–vis spectra of CdS NWs, MTC, and AMTC-LA are shown in Fig. 3a. All of the samples show a strong absorption region from 300 to 538 nm, ascribed to the CdS component, which has an intrinsic bandgap of 2.4 eV [35]. The broad absorption peak centered at 605 nm generated by both MTC and AMTC-LA samples is characteristic of the direct excitonic transitions of MoS$_2$ at the K point of the Brillouin zone [36]. Enlarged UV–vis spectra of AMTC-LA from 500 to 540 nm show detectable enhancement compared to that of MTC, which is probably

due to surface plasmon resonance of Au that enhances near-field amplitude at the resonance wavelength (Fig. 3b). The valence band (VB) XPS spectra of CdS NWs and MoS$_2$ are shown in Fig. S8, demonstrating a type I band alignment. The VB XPS spectra of AMTC are slightly shifted towards the Fermi level (EF) compared to that of MTC, which corresponds to an increase in the work function values (Fig. S9). As the junction at the MoS$_2$ and CdS interface is a Schottky contact, the charge transfer barrier (ΔE) from CdS to MoS$_2$ is significantly reduced when the MoS$_2$ tips are loaded with Au nanoparticles. A negative shift in binding energy of 0.5 eV in the Mo 3d XPS spectrum of AMTC-LA compared to that of MTC confirms the electron injection from Au to MoS$_2$ (Fig. S10) [37]. As a result, the deposition of Au on MoS$_2$ tips modifies the work function of MoS$_2$, which indirectly leads to a shift in the EF of MoS$_2$ towards a low charge transfer barrier in the MoS$_2$/CdS junction (Fig. 3c). To understand the enhanced charge carrier dynamics that arise from the Au/MoS$_2$ tips, free Au/MTC was synthesized by chemical reduction (see experimental section for details). TEM images and HAADF-TEM-energy-dispersive spectroscopy demonstrate that these Au nanoparticles have no obvious tendency to accumulate at the MoS$_2$ tips (Fig. S11). The photoluminescence (PL) decay profiles by time-correlated single-photon counting (TCSPC) experiments were characterized at low temperature (20 K). As shown in Fig. 3d, the PL decay composed of the near-band-edge (NBE) emission and the spatially localized states was expressed as τ_1 and τ_2, respectively, by biexponential fitting [23,24]. Correspondingly, τ_1 is mainly associated with the electron/hole recombination lifetime that arises from the near-band-edge emission; τ_2 originates from hole traps at deeply located states [38–40]. In the comparison of Au/MTC with AMTC-LA, the gradual increase in τ_1 from 0.98 to 1.49 ns indicates a more efficient
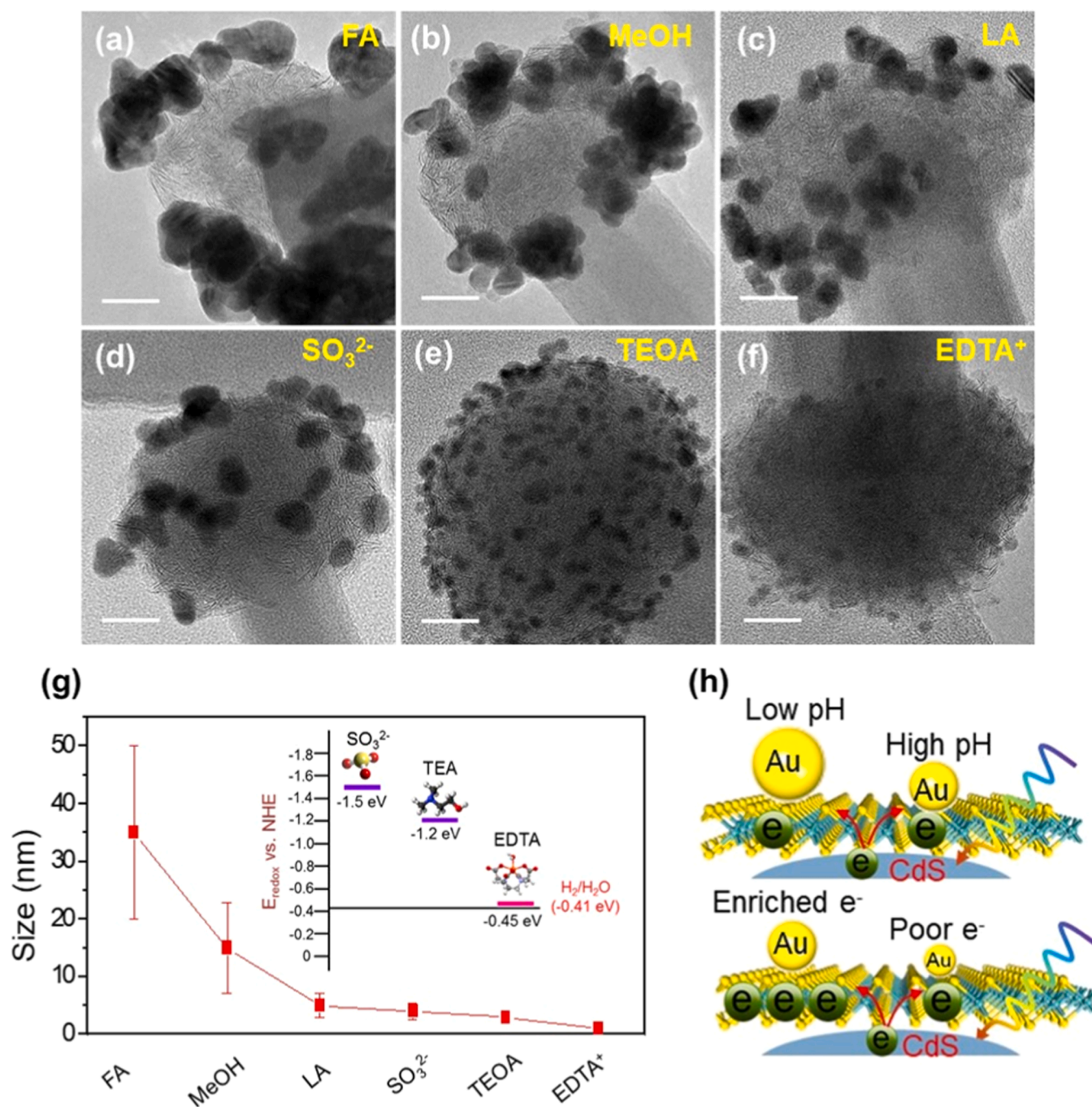
Fig. 4. (a-f) TEM images of AMTC synthesized by different hole scavengers (scan bar, 20 nm), FA, MeOH, SO_3^{2-}, LA, TEOA, and EDTA$^+$. (g) Size distributions of Au on Au/MoS$_2$ tips. (f) Possible mechanism affecting the Au particle size.

charge transfer near the CB state for AMTC. Correspondingly, the $\tau 2$ value of AMTC-LA (4.68 ns) is smaller than that of Au/MTC (5.01 ns), suggesting a change in the surface state of CdS NWs via Au loading in which the Au/CdS interface acts as another charge transfer pathway. The coexistence of Au/CdS and MoS$_2$/CdS interfaces might cause unexpected charge transfer due to the different degrees of localization of the electron wavefunction [12]. Therefore, although the change transfer from the electron acceptor (MoS$_2$) to another electron acceptor (Au) in Au/MoS$_2$ tips is complicated, the whole change transfer efficiency from CdS to Au/MoS$_2$ tips in the AMTC-LA is better than Au/MTC. As expected, the photocatalytic H$_2$ evolution activity of Au/MTC is 1.9 times lower than that of AMTC-LA when hole scavenging occurs (Fig. S12), which suggests that directionally migrating electrons accumulate at

cocatalyst tips, benefiting photocatalytic reduction.

Since Au nanoparticles were proven to selectively reduce CO_2 to CO in an aqueous solution [41,42], directional electron migration from CdS to Au/MoS$_2$ would enable not only H$_2$ evolution but also the reduction of CO_2 to CO. The ability of Au to reduce CO_2 was investigated with electrochemical polarization curves generated while bubbling 0.5 M KHCO$_3$ electrolyte with CO_2. As shown in Fig. 3e, the early appearance of cathodic currents in the CO_2-saturated electrolyte for AMTC-LA and Au/MTC is associated with the electrocatalytic CO_2 reduction activity, while the onset of CO_2 reduction in the HER is much earlier with AMTC-LA than with MTC. Furthermore, in situ DRIFTS of MTC and AMTC-LA were obtained to evaluate their CO_2 activation ability (Fig. 3f and S13). Two broad adsorption peaks at approximately 1292 and
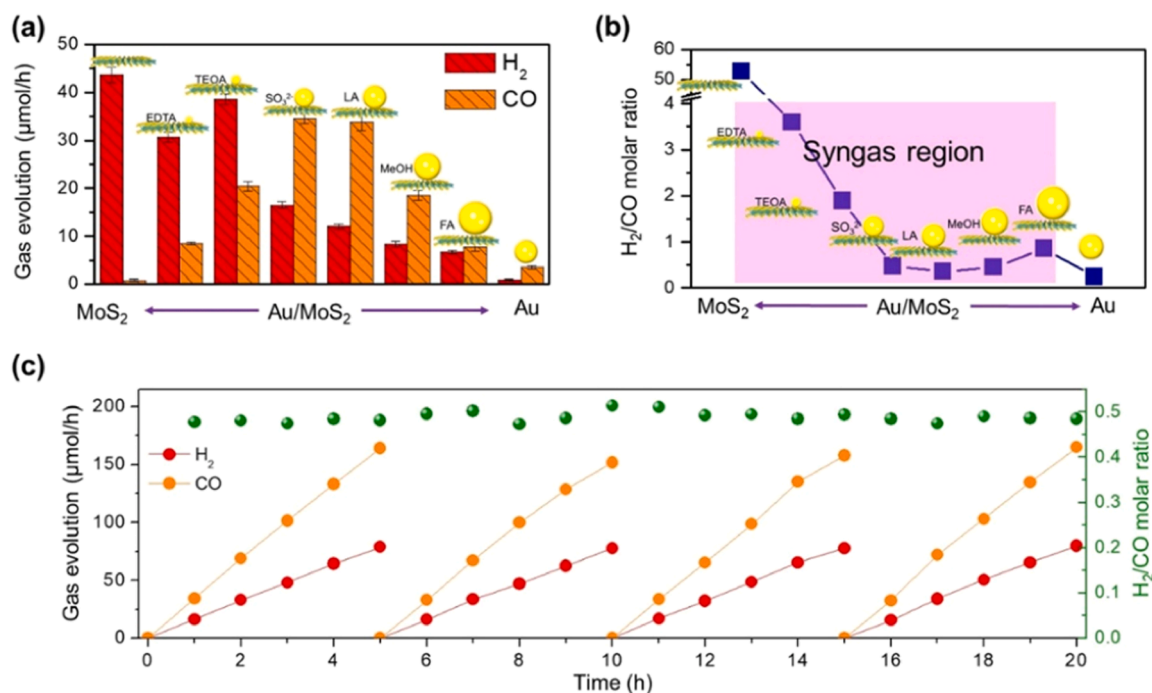
Fig. 5. Photocatalytic CO_2 reduction performance. (a) H_2/CO production ratios. (b) H_2/CO product ratios. (c) Time-dependent CO_2 reduction of AMTC-LA (conditions: 10 vol% TEOA electrolyte in 18 mL 0.5 M $KHCO_3$ electrolyte under visible light. Catalyst dosage: 0.25 mg).

1692 cm^{-1} that appeared in the DRIFTS of AMTC-LA and Au/MTC can be assigned to the characteristic vibration mode of •CO_2 [43,44], and another adsorption peak at approximately 1436 cm^{-1} can be ascribed to the asymmetric vibration of CO_3 (V_{asCO3}) resulting from the surface interaction of the adsorbed CO_2 and H_2O [45,46]. However, the temperature of CO_2 desorption for AMTC-LA is slightly increased compared to that for Au/MTC (Fig. S14), suggesting that CO_2 activation is probably enhanced by Au/MoS_2 [47]. The products of photocatalytic CO_2 reduction over AMTC-LA were primarily investigated and optimized. As shown in Fig. S15a, in a CO_2-saturated $KHCO_3$ electrolyte with different hole scavengers, including 0.5 M Na_2SO_3, 0.5 M ethylenediaminetetraacetic acid disodium salt (EDTA$^+$), 10 vol% LA or 10 vol% triethanolamine (TEOA), a 97.2% CO_2-to-CO selectivity was achieved by using TEOA, and the amount of CO evolved increased linearly, suggesting good stability (Fig. S15b). An isotope experiment using $^{13}CO_2$ as the gas source demonstrated that the CO product originated from reduction of the bubbled CO_2 (Fig. S16).

3.3. Mechanism of Au size controls

Controlling the size of the Au nanoparticles is proposed as a way to align the rates of the HER and CO_2RR for syngas generation, as the activities of the competing HER and CO_2RR were dependent on the Au particle size [47–49]. Herein, Au/MoS_2 tips with different Au particle sizes were fabricated by using different hole scavengers under photo-deposition conditions. As shown in Fig. 4a-f, in the presence of formic acid (FA), methanol (MeOH), SO_3^{2-}, LA, TEOA, and EDTA$^+$, the Au particle size distribution gradually decreased over a wide region from ~50–1 nm. The inductively coupled plasma optical emission spectroscopy (ICP-OES) results demonstrate that the $HAuCl_4$ precursors are consumed to be deposited on all MTC under the solution containing different hole scavengers (Table S1), implying that the Au amounts in all AMTC photocatalysts are similar. Because OH- groups can act as efficient capping agents to limit Au growth [50,51], the Au nanoparticles formed in the presence of alkaline hole scavengers, such as TEOA and EDTA$^+$, are smaller than those formed in the presence of acidic hole scavengers, such as FA and LA. Another possibility may occur at the

nucleation stage. At lower pH, the zeta potential of MoS_2 indicates a more negatively charged surface, which would affect Au^{3+} absorption before the photoinduced reduction (Fig. S17). In the presence of SO_3^{2-}, TEOA, and EDTA$^+$ with similar pH values (pH=8–8.3), the size difference may be caused by different oxidation potentials that give rise to different hole removal rates [52,53]. Rapid hole removal resulting from the high oxidation potential of SO_3^{2-} will enable enriched electrons to reach the MoS_2 tip, which will accelerate the photoinduced reduction and growth of Au. In contrast, EDTA$^+$, with the lowest oxidation potential, delays electron accumulation at the MoS_2 tip, thereby forming the smallest Au nanoparticles. The possible factors that influence the Au particle size are schematically depicted in Fig. 4g and h.

3.4. Photocatalytic CO_2 reduction performances

Based on the above optimized experimental conditions, syngas composition tunability was achieved over AMTCs with Au particles of different sizes in $KHCO_3$ electrolyte with 10 vol% TEOA. As shown in Fig. 5a, with no Au loading, the main product of MTC is H_2, the CO and H_2 production rates of AMTC alternate with each.

unit of evolved gas, but different total amounts of gas are evolved from the Au/MoS_2 tips of different sizes. Moreover, the Au/MoS_2 tips with Au particle sizes of 5–10 nm show high selectivity for generating CO products, while H_2 is still the dominant product over Au particles smaller than 5 nm. Remarkably, a 10 nm loading of Au alone (i.e., without MoS_2; Fig. S18) generates CO as the main product with a trace amount of H_2 and lower photocatalytic activity. These results indicate that the Au and MoS_2 as two-cocatalysts are responsible for photocatalytic CO_2 to CO conversion and HER, respectively. Moreover, the Au/MoS_2 tips can efficiently accept the photo-generated electrons from excited CdS due to the uniform interface between CdS and Au/MoS_2, which offers higher photocatalytic activity than freely loaded Au on MTC. Further on, the different sized Au particles enable changeable catalytic efficiency of CO_2RR, thereby achieving a wider region of H_2/CO ratios which can sever as the syngas with tunable composition. Fig. 5b summarizes the H_2/CO ratios over these photocatalysts: the products of AMTC are located in the syngas composition region with H_2/

CO ratios ranging from 0.35 to 3.6, whereas either MoS_2 or Au alone carry out highly efficient H_2 and CO generation. The photocatalytic activity and stability of the gas evolution ratio of AMTC-LA are given in Fig. 5c. The photocatalytic activity does not show obvious fading, and the H_2/CO ratios show slight fluctuation during consecutive cycling tests of 20 h. The AQY was calculated to be 45.55% (see detail in experimental section). Moreover, TEM images of the AMTC after long-term testing show an unchanged morphology, which means that the AMTC has high durability for photocatalytic syngas generation (Fig. S19). In addition to the tunable syngas composition, our AMTC-LA exhibits a photocatalytic CO_2-to-CO conversion performance comparable to that of CdS-based photocatalysts and a more selective photocatalytic CO_2-to-CO conversion than CdS-based photocatalysts (Table S2).

4. Conclusion

In summary, we successfully synthesized 1D CdS NWs with symmetrical Au/MoS_2 tips, where the Au nanoparticles with size ranging from 1 nm to 50 nm can be obtained in different electrolytes. Taking advantage of the spatial separation of charge carriers over the unique structure, the Au/MoS_2 tips enabled higher photocatalytic activity and tunable photocatalytic selectivity for CO_2 reduction in an aqueous solution. The Au/MoS_2-tipped CdS NWs achieved tunable syngas generation with a H_2/CO ratio ranging from 0.35 to 3.6 under visible light irradiation by simply altering the Au particle size. This new noble-metal-tipped 1D semiconductor provides another avenue for the hierarchical construction of complex structures and, consequently, tunable solar-to-fuel conversion.

CRediT authorship contribution statement

J.H.Park, L.Wang and K.Zhang conceived and designed the experiments. X.Hu, J.Jin carried out materials synthesis and data analysis, and wrote the paper. Y.Wang and C.Lin participated in part of the synthesis and analysis. S.Wan carried out mechanism analysis. All authors discussed the results and commented on the manuscript.

Declaration of Competing Interest

The authors declare that they have no known competing financial interests or personal relationships that could have appeared to influence the work reported in this paper.

Acknowledgements

Appendix A. Supporting information

Supplementary data associated with this article can be found in the online version at doi:10.1016/j.apcatb.2022.121219.

References

[1] S. Wang, X. Han, Y. Zhang, N. Tian, T. Ma, H. Huang, Inside-and-out semiconductor engineering for CO_2 photoreduction: from recent advances to new trends, Small Struct. 2 (2021), 2000061, https://doi.org/10.1002/sstr.202000061.

[2] T. Hisatomi, K. Domen, Reaction systems for solar hydrogen production via water splitting with particulate semiconductor photocatalysts, Nat. Catal. 2 (2019) 387–399, https://doi.org/10.1038/s41929-019-0242-6.

[3] K. Zhang, M. Ma, P. Li, D.H. Wang, J.H. Park, Water splitting progress in tandem devices: moving photolysis beyond electrolysis, Adv. Energy Mater. 6 (2016), 1600602, https://doi.org/10.1002/aenm.201600602.

[4] X. Li, J. Yu, M. Jaroniec, X. Chen, Cocatalysts for selective photoreduction of CO_2 into solar fuels, Chem. Rev. 119 (2019) 3962–4179, https://doi.org/10.1021/acs.chemrev.8b00400.

[5] J.H. Kim, D. Hansora, P. Sharma, J.W. Jang, J.S. Lee, Toward practical solar hydrogen production-an artificial photosynthetic leaf-to-farm challenge, Chem. Soc. Rev. 48 (2019) 1908–1971, https://doi.org/10.1039/C8CS00699G.

[6] M.B. Ross, Y.F. Li, P.D. Luna, D.H. Kim, E.H. Sargent, P.D. Yang, Electrocatalytic rate alignment enhances syngas generation, Joule 3 (2019) 257–264, https://doi.org/10.1016/j.joule.2018.09.013.

[7] P. Yang, L. Shang, J. Zhao, M. Zhang, H. Shi, H. Zhang, H. Yang, Selectively constructing nitrogen vacancy in carbon nitrides for efficient syngas production with visible light, Appl. Catal. B Environ. 297 (2021), 120946, https://doi.org/10.1016/j.apcatb.2021.120496.

[8] H.W. Zhang, J.T. Ming, J.W. Zhao, Q. Gu, C. Xu, Z.X. Ding, R.S. Yuan, Z.Z. Zhang, J.L. Long, High-rate, tunable syngas production with artificial photosynthetic cells, Angew. Chem. Int. Ed. 58 (2019) 7718–7722, https://doi.org/10.1002/anie.201902361.

[9] Q. He, D.B. Liu, J.H. Lee, Y.M. Liu, Z.H. Xie, S.Y. Hwang, S. Kattel, L. Song, J. G. Chen, Electrochemical conversion of CO_2 to syngas with controllable CO/H_2 ratios over Co and Ni single-atom catalysts, Angew. Chem. Int. Ed. 59 (2020) 3033–3037, https://doi.org/10.1002/anie.201912719.

[10] A. Li, T. Wang, X. Chang, Z.J. Zhao, C. Li, Z. Huang, P. Yang, G. Zhou, J. Gong, Tunable syngas production from photocatalytic CO_2 reduction with mitigated charge recombination driven by spatially separated cocatalysts, Chem. Sci. 9 (2018) 5334–5340, https://doi.org/10.1039/C8SC01812J.

[11] R. He, A. Zhang, Y.L. Ding, T.Y. Kong, Q. Xiao, H.L. Li, Y. Liu, J. Zeng, Achieving the widest range of syngas proportions at high current density over cadmium sulfoselenide nanorods in CO_2 electroreduction, Adv. Mater. 30 (2018) 1705872, https://doi.org/10.1002/adma.201705872.

[12] Y. Nakibli, P. Kalisman, L. Amirav, Less is more: the case of metal cocatalysts, J. Phys. Chem. Lett. 6 (2015) 2265–2268, https://doi.org/10.1021/acs.jpclett.5b00872.

[13] J. Hao, H. Liu, K. Wang, X.W. Sun, J.P. Delville, M.H. Delville, Hole scavenging and electron–hole pair photoproduction rate: two mandatory key factors to control single-tip Au–CdSe/CdS nanoheterodimers, ACS Nano 15 (2021) 15328–15341, https://doi.org/10.1021/acsnano.1c06383.

[14] W. Chen, X. Li, F. Wang, S. Javaid, Y. Pang, J. Chen, Z. Yin, S. Wang, Y. Li, G. Jia, Nonepitaxial gold-tipped ZnSe hybrid nanorods for efficient photocatalytic hydrogen production, Small 16 (2020), 1902231, https://doi.org/10.1002/smll.201902231.

[15] Y. Liu, D.A. Cullen, T. Lian, Slow auger recombination of trapped excitons enables efficient multiple electron transfer in CdS–Pt nanorod heterostructures, J. Am. Chem. Soc. 143 (2021) 20264–20273, https://doi.org/10.1021/jacs.1c09125.

[16] Y. Ben-Shahar, J.P. Philbin, F. Scotognella, L. Ganzer, G. Cerullo, E. Rabani, U. Banin, Charge carrier dynamics in photocatalytic hybrid semiconductor–metal nanorods: crossover from auger recombination to charge transfer, Nano Lett. 18 (2018) 5211–5216, https://doi.org/10.1021/acs.nanolett.8b02169.

[17] G. Zheng, S. Mourdikoudis, Z. Zhang, Plasmonic metallic heteromeric nanostructures, Small 16 (2020), e2002588, https://doi.org/10.1002/smll.202002588.

[18] J. Wu, Z. Zhang, B. Liu, Y. Fang, L. Wang, B. Dong, UV-Vis-NIR-driven plasmonic photocatalysts with dual-resonance modes for synergistically enhancing H_2 generation, Sol. RRL 2 (2018) 1800039, https://doi.org/10.1002/solr.201800039.

[19] J. Wang, T. Ding, K. Wu, Coulomb barrier for sequential two-electron transfer in a nanoengineered photocatalyst, J. Am. Chem. Soc. 142 (2020) 13934–13940, https://doi.org/10.1021/jacs.0c06256.

[20] K.F. Wu, L.J. Hill, J.Q. Chen, J.R. McBride, N.G. Pavlopolous, N.E. Richey, J. Pyun, T.Q. Lian, Universal length dependence of rod-to-seed exciton localization efficiency in type I and quasi-type II CdSe@ CdS nanorods, ACS Nano 9 (2015) 4591–4599, https://doi.org/10.1021/acsnano.5b01245.

[21] Y. Ben-Shahar, F. Scotognella, N. Waiskopf, I. Kriegel, S.D. Conte, G. Cerullo, U. Banin, Effect of surface coating on the photocatalytic function of hybrid CdS-Au nanorods, Small 11 (2015) 462–471, https://doi.org/10.1002/smll.201402262.

[22] P. Kalisman, Y. Nakibli, L. Amirav, Perfect photon-to-hydrogen conversion efficiency, Nano Lett. 16 (2016) 1776, https://doi.org/10.1021/acs.nanolett.5b04813.

[23] K. Zhang, J.K. Kim, M. Ma, S.Y. Yim, C.L. Lee, H.J. Shin, J.H. Park, Delocalized electron accumulation at nanorod tips: origin of efficient H_2 generation, Adv. Funct. Mater. 26 (2016) 4527–4534, https://doi.org/10.1002/adfm.201600285.

[24] K. Zhang, S.F. Qian, W.J. Kim, J.K. Kim, X.W. Sheng, J.Y. Lee, J.H. Park, Double 2-dimensional H_2-evolving catalyst tipped photocatalyst nanowires: a new avenue for high-efficiency solar to H_2 generation, Nano Energy 34 (2017) 481–490, https://doi.org/10.1016/j.nanoen.2017.03.005.

[25] B.H. Wu, D.Y. Liu, S. Mubeen, T.T. Chuong, M. Moskovits, G.D. Stucky, Anisotropic growth of TiO_2 onto gold nanorods for plasmon-enhanced hydrogen production

from water reduction, J. Am. Chem. Soc. 138 (2016) 1114, https://doi.org/10.1021/jacs.6b02755.

[26] J.Y. Choi, W.-W. Park, B. Park, S. Sul, O.-H. Kwon, H. Song, Optimal length of hybrid metal–semiconductor nanorods for photocatalytic hydrogen generation, ACS Catal. 11 (2021) 13303–13311, https://doi.org/10.1021/acscatal.1c03754.

[27] A. Manzi, T. Simon, C. Sonnleitner, M. Doblinger, R. Wyrwich, O. Stern, J. K. Stolarczyk, J. Feldmann, Light-induced cation exchange for copper sulfide based CO₂ reduction, J. Am. Chem. Soc. 137 (2015) 14007–14010, https://doi.org/10.1021/jacs.5b06778.

[28] E. Aronovitch, P. Kalisman, L. Houben, L. Amirav, M. Bar-Sadan, Stability of seeded rod photocatalysts: atomic scale view, Chem. Mater. 28 (2016) 1546–1552, https://doi.org/10.1021/acs.chemmater.6b00040.

[29] T. Chen, F. Tong, J. Enderlein, Z. Zheng, Plasmon-driven modulation of reaction pathways of individual Pt modified Au nanorods, Nano Lett. 20 (2020) 3326–3330, https://doi.org/10.1021/acs.nanolett.0c00206.

[30] S.J.P. Varapragasam, S. Mia, C. Wieting, C. Balasanthiran, M.Y. Hossan, A. Baride, R.M. Rioux, J.D. Hoefelmeyer, Ag–TiO₂ hybrid nanocrystal photocatalyst: hydrogen evolution under UV irradiation but not under visible-light irradiation, ACS Appl. Energy Mater. 2 (2019) 8274–8282, https://doi.org/10.1021/acsaem.9b01730.

[31] K. Dong, Q.-C. Chen, Z. Xing, Y. Chen, Y. Qi, N.G. Pavlpoulos, L. Amirav, Silver tipping of CdSe@CdS nanorods: how to avoid cation exchange, Chem. Mater. 33 (2021) 6394–6402, https://doi.org/10.1021/acs.chemmater.1c01598.

[32] B. Shen, L. Huang, J. Shen, L. Meng, E.J. Kluender, C. Wolverton, B. Tian, C. A. Mirkin, Synthesis of metal-capped semiconductor nanowires from heterodimer nanoparticle catalysts, J. Am. Chem. Soc. 142 (2020) 18324–18329, https://doi.org/10.1021/jacs.0c09222.

[33] X.H. Li, J. Lian, M. Lin, Y.T. Chan, Light-induced selective deposition of metals on gold-tipped CdSe-seeded CdS nanorods, J. Am. Chem. Soc. 133 (2011) 672–675, https://doi.org/10.1021/ja1076603.

[34] M. Murdoch, G.I.N. Waterhouse, M.A. Nadeem, J.B. Metson, M.A. Keane, R. F. Howe, J. Llorca, H. Idriss, The effect of gold loading and particle size on photocatalytic hydrogen production from ethanol over Au/TiO₂ nanoparticles, Nat. Chem. 3 (2011) 489–492, https://doi.org/10.1038/NCHEM.1048.

[35] J. Jin, J.G. Yu, G. Liu, P.K. Wong, Single crystal CdS nanowires with high visible-light photocatalytic H₂-production performance, J. Mater. Chem. A 1 (2013) 10927–10934, https://doi.org/10.1039/c3ta12301d.

[36] G.J. Guan, S.Y. Zhang, S.H. Liu, Y.Q. Cai, M. Low, C.P. Teng, I.Y. Phang, Y. Cheng, K.L. Duei, B.M. Srinivasan, Y.G. Zheng, Y.W. Zhang, M.Y. Han, Protein induces layer-by-layer exfoliation of transition metal dichalcogenides, J. Am. Chem. Soc. 137 (2015) 6152–6155, https://doi.org/10.1021/jacs.5b02780.

[37] S. Suna, Q. An, M. Watanabe, J. Cheng, H.H. Kim, T. Akbay, A. akagaki, T. Ishihar, Highly correlation of CO₂ reduction selectivity and surface electron Accumulation: A case study of Au-MoS₂ and Ag-MoS₂ catalyst, Appl. Catal. B Environ. 271 (2020), 118931, https://doi.org/10.1016/j.apcatb.2020.118931.

[38] L.V. Titova, T.B. Hoang, H.E. Jackson, L.M. Smith, Low-temperature photoluminescence imaging and time-resolved spectroscopy of single CdS nanowires, Appl. Phys. Lett. 89 (2006), 053119, https://doi.org/10.1063/1.2266414.

[39] B. Tian, W. Gao, X. Zhang, Y. Wu, G. Lu, Water splitting over core-shell structural nanorod CdS@Cr₂O₃ catalyst by inhibition of H₂-O₂ recombination via removing nascent formed oxygen using perfluorodecalin, Appl. Catal. B Environ. 221 (2018) 618–625, https://doi.org/10.1016/j.apcatb.2017.09.065.

[40] K. Zhang, J.K. Kim, B. Park, S. Qian, B. Jin, X. Sheng, H. Zeng, H. Shin, S.H. Oh, C. L. Lee, J.H. Park, Defect-induced epitaxial growth for efficient solar hydrogen production, Nano Lett. 17 (2017) 6676–6683, https://doi.org/10.1021/acs.nanolett.7b02622.

[41] D.R. Yang, L. Liu, Q. Zhang, Y. Shi, Y. Zhou, C. Liu, F.B. Wang, X.H. Xia, Importance of Au nanostructures in CO₂ electrochemical reduction reaction, Sci. Bull. 65 (2020) 796–802, https://doi.org/10.1016/j.scib.2020.01.015.

[42] Y.H. Chen, C.W. Li, M.W. Kanan, Aqueous CO₂ reduction at very low overpotential on oxide-derived Au nanoparticles, J. Am. Chem. Soc. 134 (2012) 19969–19972, https://doi.org/10.1021/ja309317u.

[43] J. Wu, X.D. Li, W. Shi, P.Q. Ling, Y.F. Sun, X.C. Jiao, S. Gao, L. Liang, J.Q. Xu, W. S. Yan, C.M. Wang, Y. Xie, Efficient Visible-light-driven CO₂ reduction mediated by defect-engineered BiOBr atomic layers, Angew. Chem. Int. Ed. 57 (2018) 8719–8723, https://doi.org/10.1002/anie.201803514.

[44] M. Wang, M. Shen, X.X. Jin, J.J. Tian, M.L. Li, Y.J. Zhou, L.X. Zhang, Y.S. Li, J. L. Shi, Oxygen vacancy generation and stabilization in CeO₂₋ₓ by Cu introduction with improved CO₂ photocatalytic reduction activity, ACS Catal. 9 (2019) 4573–4581, https://doi.org/10.1021/acscatal.8b03975.

[45] A. Zhang, R. He, H.P. Li, Y.J. Chen, T.Y. Kong, K. Li, H.X. Ju, J.F. Zhu, W.G. Zhu, J. Zeng, Nickel doping in atomically thin tin disulfide nanosheets enables highly efficient CO₂ reduction, Angew. Chem. Int. Ed. 57 (2018) 10954–10958, https://doi.org/10.1002/anie.201806043.

[46] X.D. Li, Y.F. Sun, J.Q. Xu, Y.J. Shao, J. Wu, X.L. Xu, Y. Pan, H.X. Ju, J.F. Zhu, Y. Xie, Selective visible-light-driven photocatalytic CO₂ reduction to CH₄ mediated by atomically thin CuIn5S8 layers, Nat. Energy 4 (2019) 690–699, https://doi.org/10.1038/s41560-019-0431-1.

[47] J.P. Sheng, Y. He, J.Y. Li, C.W. Yuan, H.W. Huang, S.Y. Wang, Y.J. Sun, Z.M. Wang, F. Dong, Identification of halogen-associated active sites on bismuth-based perovskite quantum dots for efficient and selective CO₂-to-CO photoreduction, ACS Nano 14 (2020) 13103–13114, https://doi.org/10.1021/acsnano.0c04659.

[48] W.L. Zhu, R. Michalsky, O. Metin, H.F. Lv, S.J. Guo, C.J. Wright, X.L. Sun, A. A. Peterson, S.H. Sun, Monodisperse Au nanoparticles for selective electrocatalytic reduction of CO2 to CO, J. Am. Chem. Soc 135 (2013) 16833–16836, https://doi.org/10.1021/jacs.7b05685.

[49] H. Mistry, R. Reske, Z.H. Zeng, Z.J. Zhao, J. Greeley, P. Strasser, B.R. Cuenya, Exceptional size-dependent activity enhancement in the electroreduction of CO₂ over Au nanoparticles, J. Am. Chem. Soc. 136 (2014) 16473–16476, https://doi.org/10.1021/ja508879j.

[50] J.A. Trindell, J. Clausmeyer, R.M. Crooks, Size stability and H₂/CO selectivity for Au nanoparticles during electrocatalytic CO₂ reduction, J. Am. Chem. Soc. 139 (2017) 16161–16167, https://doi.org/10.1021/jacs.7b06775.

[51] X.H. Ji, X.N. Song, J. Li, Y.B. Bai, W.S. Yang, X.G. Peng, Size control of gold nanocrystals in citrate reduction: the third role of citrate, J. Am. Chem. Soc. 129 (2007) 13939–13948, https://doi.org/10.1021/ja074447k.

[52] F. Shiba, Size control of monodisperse Au nanoparticles synthesized via a citrate reduction process associated with a pH-shifting procedure, CrystEngComm 15 (2013) 8412–8415, https://doi.org/10.1039/c3ce41516c.

[53] Y.L. Jia, Z.H. Wang, L.Y. Wang, Y. Ma, G.N. Wang, Y.H. Lin, X. Hu, K. Zhang, Awakening solar hydrogen evolution of MoS₂ in alkalescent electrolyte through doping with Co, ChemSusChem 12 (2019) 3336–3342, https://doi.org/10.1002/cssc.201900936.